



A Multiwavelength Study of the Cool Core Cluster MACS J1447.4+0827

M. Prasow-Émond¹, J. Hlavacek-Larrondo¹, C. L. Rhea¹, M. Latulippe¹, M.-L. Gendron-Marsolais^{1,2},
A. Richard-Laferrrière^{1,3}, J. S. Sanders⁴, A. C. Edge⁵, S. W. Allen^{6,7}, A. Mantz^{6,7}, and A. von der Linden⁸

¹Département de Physique, Université de Montréal, C.P. 6128, Succ. Centre-Ville, Montréal, QC H3C 3J7, Canada; myriampe@astro.umontreal.ca

²European Southern Observatory, Alonso de Córdova 3107, Vitacura, Casilla 19001, Santiago, Chile

³Institute of Astronomy, University of Cambridge, Madingley Road, Cambridge, CB3 0HA, UK

⁴Max-Planck-Institut für extraterrestrische Physik, D-85748 Garching, Germany

⁵Institute of Computational Cosmology, Department of Physics, Durham University, Durham, DH1 3LE, UK

⁶Department of Physics, Stanford University, 452 Lomita Mall, Stanford, CA 94305-4085, USA

⁷Kavli Institute for Particle Astrophysics and Cosmology, Stanford University, 382 Via Pueblo Mall, Stanford, CA 94305-4060, USA

⁸Department of Physics and Astronomy, Stony Brook University, Stony Brook, NY 11794, USA

Received 2019 November 25; revised 2020 June 8; accepted 2020 June 17; published 2020 August 7

Abstract

Clusters of galaxies are outstanding laboratories for understanding the physics of supermassive black hole (SMBH) feedback. Here we present the first Chandra, Karl G. Jansky Very Large Array, and Hubble Space Telescope analysis of MACS J1447.4+0827 ($z = 0.3755$), one of the strongest cool core clusters known, in which extreme feedback from its central SMBH is needed to prevent the hot intracluster gas from cooling. Using this multiwavelength approach, including 70 ks of Chandra X-ray observations, we detect the presence of collimated jetted outflows that coincide with a southern and a northern X-ray cavity. The total mechanical power associated with these outflows ($P_{\text{cav}} \approx 6 \times 10^{44} \text{ erg s}^{-1}$) is roughly consistent with the energy required to prevent catastrophic cooling of the hot intracluster gas ($L_{\text{cool}} = 1.71 \pm 0.01 \times 10^{45} \text{ erg s}^{-1}$ for $t_{\text{cool}} = 7.7 \text{ Gyr}$), implying that powerful SMBH feedback was in place several Gyr ago in MACS J1447.4+0827. In addition, we detect the presence of a radio minihalo that extends over 300 kpc in diameter ($P_{1.4\text{GHz}} = 3.0 \pm 0.3 \times 10^{24} \text{ W Hz}^{-1}$). The X-ray observations also reveal an $\sim 20 \text{ kpc}$ plumelike structure that coincides with optical dusty filaments that surround the central galaxy. Overall, this study demonstrates that the various physical phenomena occurring in the most nearby clusters of galaxies are also occurring in their more distant analogs.

Unified Astronomy Thesaurus concepts: Black hole physics (159); High energy astrophysics (739); Active galactic nuclei (16); Radio jets (1347); Relativistic jets (1390); Galaxy clusters (584); X-ray astronomy (1810); Hubble Space Telescope (761); Optical observatories (1170)

Supporting material: data behind figures

1. Introduction

Clusters of galaxies are the largest gravitationally bound structures in the universe. They are primarily composed of dark matter and an intracluster medium (ICM). They also contain hundreds to thousands of galaxies, including some of the most massive galaxies in the universe. At the center, a giant galaxy usually stands out, known as the brightest cluster galaxy (BCG). The BCG is generally an elliptical galaxy hosting, at its center, a supermassive black hole (SMBH) that can generate powerful outflow jets (e.g., McConnell et al. 2011).

We generally classify clusters into two categories based on the spatial distribution of the hot ICM: cool core clusters, where the X-ray surface brightness distribution peaks steeply toward the center and the temperature drops abruptly in the core by a factor of ~ 2 – 3 , and non-cool core clusters, in which the X-ray surface brightness distribution is less peaked and more uniform. In the centers of cool core clusters, the optically thin, almost completely ionized ICM has a radiative cooling time that is remarkably short ($\ll 10^9 \text{ yr}$; e.g., Voigt & Fabian 2004; Peterson & Fabian 2006; Hlavacek-Larrondo et al. 2012b). Left to its own devices, this gas would be forecast to cool and form stars at rates of several hundred to thousands of solar masses per year (e.g., Fabian 1994). However, the ICM is not cooling as fast as predicted; therefore, the observed star formation rates are much lower than expected (e.g., Johnstone et al. 1987; Nulsen et al. 1987; O’Dea et al. 2008; Rafferty et al. 2008; Gaspari et al. 2013a; McDonald et al. 2018).

This discrepancy is likely due to the active galactic nucleus (AGN) located at the center of the BCG through a mechanism known as AGN feedback. According to this mechanism, the AGN inflates cavities (or bubbles) in the ICM, detectable using X-ray emission, through relativistic jetted outflows visible at radio wavelengths. The exact mechanism that uniformly reheats the ICM is not yet known, although shock, sound waves, and turbulent heating are likely part of the process (e.g., Birzan et al. 2004, 2008; Dunn & Fabian 2006, 2008; Nulsen et al. 2009; Cavagnolo et al. 2010; Dong et al. 2010; Hlavacek-Larrondo et al. 2012b; Zhuravleva et al. 2014, 2016, 2018).

The goal of this paper is to better understand these AGN processes by targeting one of the most massive and strongest cool core clusters known, in which feedback must be operating at an extreme level to offset cooling. The MASSive Cluster Survey (MACS) consists of a sample of about 120 very X-ray luminous clusters located at a redshift between 0.3 and 0.7 (e.g., Ebeling et al. 2001, 2007, 2010). The clusters were selected from the ROSAT All-Sky Survey and spectroscopically confirmed. MACS has allowed the discovery of new massive clusters at $z > 0.3$ and thus improved the ability to study their evolution, as well as the physical and cosmological parameters driving them. MACS clusters have also been the focus of several gravitational lensing surveys (e.g., MACS J0416.1–2403, Kaurov et al. 2019; MACS J0717.5+3745, Zitrin et al. 2009; Jauzac et al. 2012; Limousin et al. 2012; MACS J1149.5+2223, Smith et al. 2009; MACS

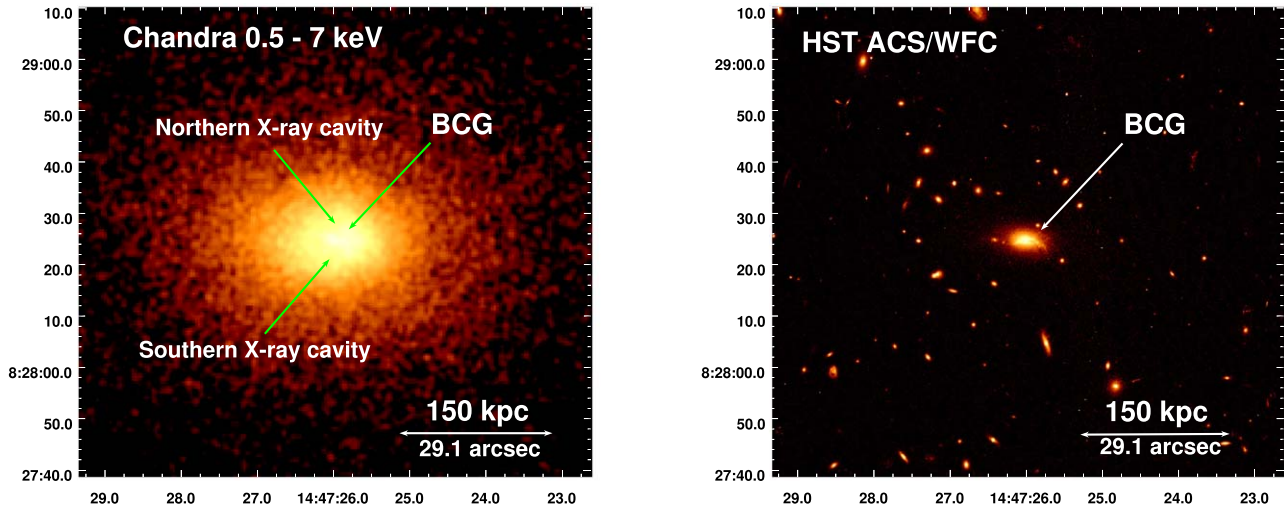


Figure 1. Left: cleaned, exposure-corrected, and background-subtracted 0.5–7 keV Chandra image of MACS J1447.4+0827. The total exposure time is 76.3 ks, and the image has been smoothed with a $\sigma = 2$ Gaussian function. We highlighted the position of two X-ray cavities, although they are not visible in the raw image, for reference (see Section 3 for evidence of their existence). The location of the BCG is also shown. Right: same-scale HST ACS/WFC F814W image centered on the BCG.

Table 1
Chandra Observations

Observation Number	Date	Detector	Exposure (ks)
10481	2008 Dec 14	ACIS-S	11.1
17233	2016 Apr 5	ACIS-I	41.0
18825	2016 Apr 6	ACIS-I	24.2

J0416.1–2403, Chirivì et al. 2018; Weighing the Giants program, Applegate et al. 2014, 2016; von der Linden et al. 2014).

In this paper, we present a multiwavelength study of MACS J1447.4+0827 ($z = 0.3755$), one of the strongest and most X-ray-luminous cool core clusters in MACS, similar to well-studied systems such as RBS 797 (e.g., Schindler et al. 2001; Jetzer et al. 2002; Castillo-Morales & Schindler 2003; Gitti et al. 2006), MACS J1931.8–2634 (e.g., Ehlert et al. 2011; Santos et al. 2016), IRAS 09104+4109 (e.g., Kleinmann et al. 1988; Hines & Wills 1993; Franceschini et al. 2000; Iwasawa et al. 2001; Piconcelli et al. 2007; Vignali et al. 2011; Farrah et al. 2016), and RX J1532.9+3021 (e.g., Hlavacek-Larrondo et al. 2013a; Gupta et al. 2016). Here we present the first detailed study of this cluster. This paper is based on new Chandra X-ray Observatory and Karl G. Jansky Very Large Array (JVLA) observations of the source and focuses on understanding its feedback properties. Richard-Laferrrière et al. (2020) recently presented the radio mini-halo properties of this cluster.

Section 2 introduces the X-ray, radio, and optical observations and the data reduction and processing. Section 3 presents the X-ray imaging analysis of the cluster. Section 4 presents a detailed X-ray spectral analysis of the thermodynamic properties of MACS J1447.4+0827. In Section 5, we present the radio analysis of the cluster. In Section 6, we highlight the properties of the central AGN. Finally, in Section 7, we discuss our results and their implications.

We use $H_0 = 70 \text{ km s}^{-1} \text{ Mpc}^{-1}$, $\Omega_m = 0.3$, and $\Omega_\Lambda = 0.7$ as values of the cosmological parameters and $z = 0.3755$ as the

cluster redshift ($1'' = 5.157 \text{ kpc}$; Ebeling et al. 2010). Errors are 1σ (68.3%) throughout the paper (unless mentioned).

2. Observations and Data Reduction

2.1. X-Rays: Chandra Observations

The Chandra Advanced CCD Imaging Spectrometer (ACIS) in VFaint mode was used to observe MACS J1447.4+0827 three times: first in 2008, centered on the ACIS-S3 back-illuminated chip (12 ks, ObsID 10481; PI: Hicks), and then twice in 2016, centered on the ACIS-I3 front-illuminated chip (43 ks, ObsID 17233; and 25 ks, ObsID 18825; PI: Hlavacek-Larrondo). These observations are presented in Table 1.

Starting from the event 1 file, the ObsIDs were cleaned, processed, and calibrated using the CIAO software (CIAO v4.10 and CALDB v4.7.8). After reprocessing the data with the `chandra_repro` routine, we excluded nine point sources by eye using `ds9`, and we removed flares with `deflare` with `lc_clean` and a 3σ threshold. The net exposure times are presented in Table 1.

Background event files, background images, and background-subtracted images were generated using `blanksky` and `blanksky_image`. Finally, the tool `merge_obs` was applied to the observations to merge the event files, which created a final exposure-corrected image. The cleaned, merged, background-subtracted, and exposure-corrected Chandra image is presented in the left panel of Figure 1. We note that we also computed several of the cluster properties using a background region far from the cluster on the ACIS-I chips and obtained consistent results with the `blanksky` background event files.

We used XSPEC (v12.10.0c) to spectroscopically analyze the X-ray observations of MACS J1447.4+0827. Throughout this study, we used the Anders & Grevesse (1989) abundance ratios and the Kalberla et al. (2005) value of the Galactic absorption ($n_h = 0.0224 \times 10^{22} \text{ cm}^{-2}$). We verified this value by picking a certain region located between 50 and 200 kpc from the center—in which there is no emission (e.g., from the AGN)—and fitting an absorbed `apep` plasma model to the spectrum in the 0.5–7 keV energy range while leaving the Galactic absorption, temperature, abundance, and normalization parameters free

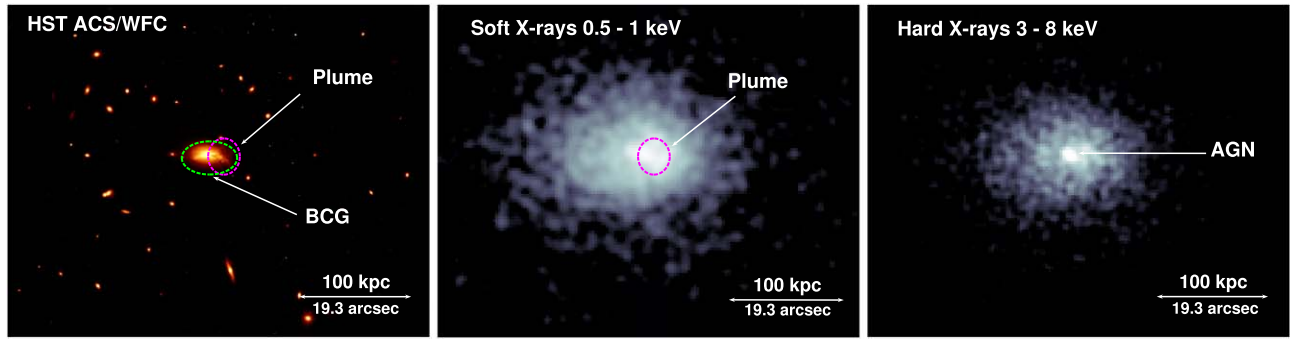


Figure 2. Left: HST ACS/WFC F814W image centered on the BCG, same as the right panel of Figure 1. The BCG has been circled by a green ellipse and the plume structure by a magenta ellipse. Middle: soft 0.5–1 keV Chandra image of MACS J1447.4+0827. The image has been smoothed with a $\sigma = 2$ Gaussian function, and this is the kernel that best highlights the feature. The plumelike structure is indicated by the same magenta ellipse. Right: same-scale hard 3–8 keV Chandra image, where the AGN location is indicated. The image has been smoothed with a $\sigma = 2$ Gaussian function.

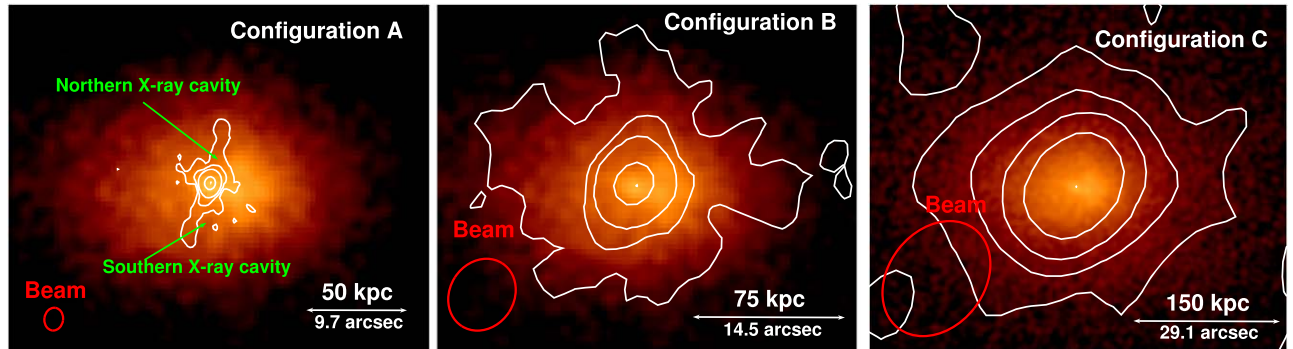


Figure 3. Left: background-subtracted and exposure-corrected 0.5–7 keV Chandra image (same as Figure 1) with 1.4 GHz JVLA contours of the configuration A observations. The contours are $4\sigma_{\text{rms}} = 0.044, 0.176, 0.704, 5, \text{ and } 35 \text{ mJy beam}^{-1}$. The beam is $0''.9 \times 1''.1$ and has a position angle from north to east of $-7^\circ 73'$. The locations of the northern and southern X-ray cavities are indicated for reference (see Section 3 for evidence of their existence). Middle: same as left panel but with contours of the configuration B observations. The contours are $4\sigma_{\text{rms}} = 0.064, 0.3, 1, 5, \text{ and } 35 \text{ mJy beam}^{-1}$. The beam is $3''.1 \times 3''.6$ and has a position angle from north to east of $-32^\circ 7'$. Right: same as left panel but with contours of the configuration C observations. The contours are $4\sigma_{\text{rms}} = 0.060, 0.3, 1, 5, \text{ and } 39 \text{ mJy beam}^{-1}$. The beam is $9''.6 \times 12''.5$ and has a position angle from north to east of $-37^\circ 8'$.

Table 2
JVLA Radio Observations

Date	Frequency (GHz)	Bandwidth (GHz)	Configuration	Duration (minutes)	σ_{rms} (mJy beam $^{-1}$)
2015 Aug 14	1.5	1	A	180	0.011
2016 May 25	1.5	1	B	180	0.016
2016 Feb 2	1.5	1	C	180	0.015

to vary. We obtained results consistent with the Kalberla et al. (2005) value within 1σ .

The middle and right panels of Figure 2 present the soft 0.5–1 keV and hard 3–8 keV X-ray Chandra images. The middle panel reveals a plumelike structure that matches the western filaments of the BCG, which we discuss in Section 4.3. The right panel has a bright pointlike region in the center coincident with the BCG. We interpret this feature as the central AGN, and we present its properties in Section 6.

2.2. Radio: JVLA Observations

MACS J1447.4+0827 was also observed with the JVLA at 1.4 GHz (*L* band; PI: Hlavacek-Larrondo). We present a summary of the data in Table 2. Configurations A, B, and C were obtained to maximize the different scales detected; the A-configuration observations are of comparable resolution to Chandra, whereas the B and C configurations allow for better

detection of faint extended radio emission. The data were reduced with the software CASA (v4.6). A more detailed description of the data reduction and imaging processes is presented in Richard-Laferrière et al. (2020).

The exposure-corrected and background-subtracted 0.5–7 keV Chandra image and the 1.4 GHz JVLA configuration A (left), B (middle), and C (right) contours are shown in Figure 3. The images have beam sizes of $0''.9 \times 1''.1$, $3''.1 \times 3''.6$, and $9''.6 \times 12''.5$, respectively. The rms values reached are shown in Table 2.

The A-configuration contours reveal the presence of a compact central AGN that coincides with the X-ray point source seen in the right panel of Figure 2 and located at R.A. = $14^{\text{h}}47^{\text{m}}26^{\text{s}}.022$ and decl. = $+8^\circ 28' 25''.26$. It also reveals the presence of jetted outflows oriented north–south that will be analyzed in Section 6.3. Configurations B and C reveal faint emission that extends out to ~ 160 kpc of radius.

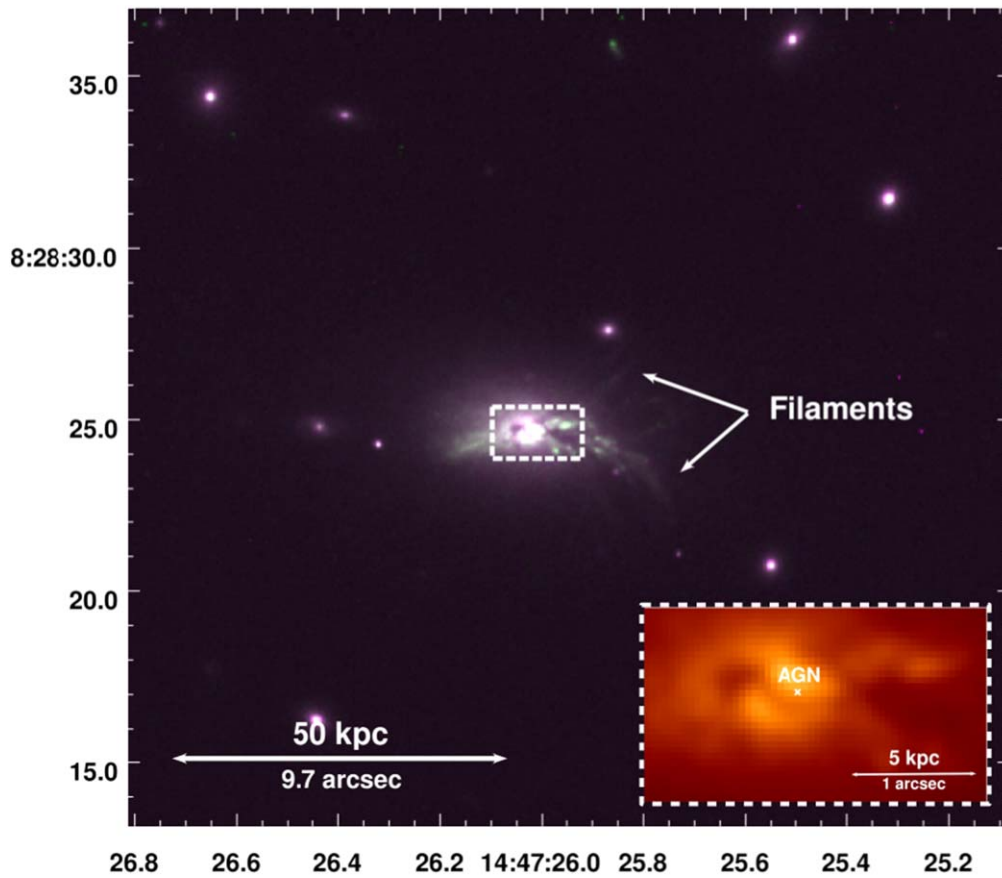


Figure 4. Combined HST F814W (red and blue) and F606W (green) images centered on the BCG of MACS J1447.4+0827. The inset at the bottom right is a zoom on the central part of the galaxy focusing on the optical nucleus and shows the position of the AGN as detected at 1.4 GHz based on the A-configuration JVLA observations.

This type of structure has already been seen in other cool core clusters, and we interpreted it as a radio minihalo (e.g., Mazzotta & Giacintucci 2008; Richard-Laferrrière et al. 2020). We characterize the properties of the minihalo in Section 5.2.

2.3. Optical: HST Observations

The Hubble Space Telescope (HST) was used to provide optical images of MACS J1447.4+0827 (PI: Ebeling). We used two broadband filters both using the camera Wide Field Channel (WFC)/HRC: F606W ($\lambda = 5907 \text{ \AA}$; $\Delta\lambda = 2342 \text{ \AA}$) and F814W ($\lambda = 8333 \text{ \AA}$; $\Delta\lambda = 2511 \text{ \AA}$). These filters contain the redshifted $H\alpha$ emission line ($H\alpha \lambda 6562$) and highlight the filamentary structure of the BCG. The right panel of Figure 1 and the left panel of Figure 2 show the F814W image taken with the Advanced Camera for Surveys (ACS) WFC.

Figure 4 shows the combined HST F814W (red and blue) and F606W (green) images of MACS J1447.4+0827. The BCG is surrounded by optically bright filaments up to $\sim 25 \text{ kpc}$ in size. We can denote two prominent filaments: one oriented in the west–south direction and one oriented in the west–north direction. We analyze the properties of the filaments in more detail in Section 7.2.

3. X-Ray Imaging Analysis of the Cluster

In the following sections, we present the methods used in this study to highlight the X-ray cavities. Although the cavities are not clearly visible in the raw image (see Figure 1), they

must exist due to the presence of relativistic outflows (see left panel of Figure 3) that push gas. We therefore applied a total of three different methods to bring out these features.

3.1. Gaussian Gradient Magnitude

First, we applied a Gaussian gradient magnitude (GGM) filter technique that has recently been applied to astronomical X-ray data sets (Sanders et al. 2016). Starting with the exposure-corrected, background-subtracted image of MACS J1447.4+0827, we convolve the image with the multidirectional gradient of a Gaussian using the `scipy` implementation.⁹ This process allows us to strategically resolve astrophysical phenomena of different scale lengths by adjusting the Gaussian’s sigma value. Here we have chosen $\sigma = 2$ in order to pick out structures corresponding to a 5 kpc scale. We further applied a logarithmic scaling to highlight the complicated substructure. We present the GGM Chandra image in the left panel of Figure 5. Unfortunately, we do not detect any cavities with this technique, but this image allows to see the variations in the cluster.

3.2. Unsharp-masked

We then subtracted a 2D Gaussian smoothed image ($\sigma = 6$ pixels) from a less smoothed image ($\sigma = 1$ pixel) using `fgauss` and `farith` from CIAO. This unsharp-masked

⁹ The implementation of our code can be found at <https://github.com/crhea93/AstronomyTools/tree/master/GGF>.

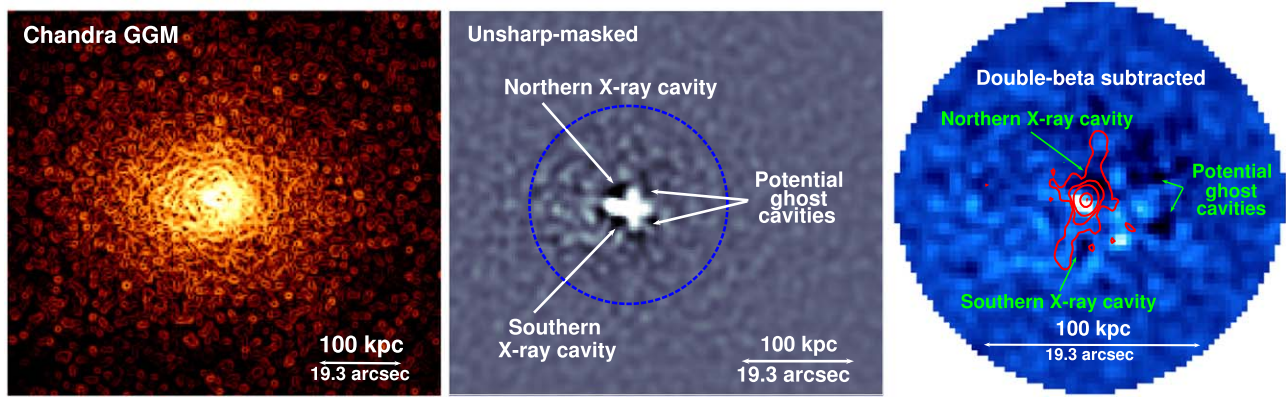


Figure 5. Left: background-subtracted and exposure-corrected 0.5–7 keV Chandra image, same as Figure 1, but with a GGM filter with $\sigma = 2$. This image allows us to better detect the complicated substructure. The spirals are caused by point sources. Middle: unsharp-masked Chandra image, where a 2D Gaussian image ($\sigma = 6$) was subtracted from a less smoothed image ($\sigma = 1$; see Section 3.2). Different features are highlighted. The blue circle indicates the size of the double- β image (right panel). Right: smoothed image (2D Gaussian with $\sigma = 2$) subtracted from a double- β model (see Section 3.3). The X-ray cavities and potential X-ray ghost cavities are indicated. We added the 1.4 GHz JVLA contours in the A configuration, same as Figure 3.

image is presented in the middle panel of Figure 5, where we can denote four cavity-like structures. In the middle of this image, we can also see a brightest part—a plumelike structure—that will be described in Section 4.3. We tested several smoothing and binning factors to make the X-ray cavities as clear as possible.

3.3. Double- β Model

To further test the presence of cavities, we used a double- β model (e.g., Jones & Forman 1984; Vikhlinin et al. 2005) to fit the X-ray surface brightness profile based on the following equation from Cavaliere & Fusco-Femiano (1976):

$$S(r) = S_{01} \left(1 + \left(\frac{r}{r_{c1}} \right)^2 \right)^{-3\beta_1+0.5} + S_{02} \left(1 + \left(\frac{r}{r_{c2}} \right)^2 \right)^{-3\beta_2+0.5} + C. \quad (1)$$

Here S_0 is the central surface luminosity, r_c is the radius of the core, β is the slope, and C is the constant associated with the background.

To create the model, we initially divided a circular region of 100 kpc from the center into 15 equal sectors, and each section was separated in 40 radial ranges. We then extracted the surface brightness of the radial ranges from each sector with the tool `dmextract` from CIAO. The double- β model was fitted to those regions, which produced a brightness profile for every sector. The model was created by assembling the 15 sectors by smoothing over the sharp discontinuities at the edges of the sectors using `fgauss`. Finally, we subtracted the model image from the original image. We present the results in the right panel of Figure 5, in which we added the contours of the JVLA A-configuration observations. Note that we varied the parameters (number of regions, coordinates of the center, and number of regions per sector) and obtained results consistent with the unsharp-masked image in the previous subsection. Figure 5 reveals northern and southern potential cavities but also two potential ghost cavities consisting of cavities that have been dragging out of the AGN’s area to larger radii. To test the presence of the northern and southern cavities, we fitted the double- β model along four regions and obtained surface

brightness profiles in Figure 6. The northern cavity is detected at 2σ and the southern at 1.7σ . These detections are statistically weak compared to others clusters (an X-ray cavity surface brightness is normally $\sim 20\%$ below the ICM’s), but we can still confirm the presence of two X-ray cavities due to the presence of the relativistic outflows. We further discuss this interesting feature in Section 7.2.

We note that the 1.4 GHz JVLA emission matches the position of the northern potential cavity but does not exactly match the southern cavity. Located further away from the AGN, ghost cavities are filled with radio emission with steeper spectra as their relativistic electron content got older and are therefore less bright at 1.4 GHz than the inner cavities. They are also more difficult to see in the X-ray due to the decreasing brightness as a function of the radius. The X-ray energetics of the cavities will be presented in Section 6.3 and we further discuss the presence of the potential ghost cavities in Section 7.3.

4. X-Ray Spectral Analysis of the Cluster

The following sections present the thermodynamic profiles and maps of the cluster.

4.1. Thermodynamic Profiles

To compute the thermodynamic profiles, we selected nine elliptical regions of ~ 6000 counts with a signal-to-noise ratio of ~ 75 centered on the central AGN from the background-subtracted image. To determine the ellipticity (ϵ) of these regions, we manually traced elliptical regions on the X-ray image on 10 contours smoothed with a $\sigma = 10$ Gaussian function. These regions encompass all of the X-ray emission up to a distance of ~ 750 kpc from the center, and the ellipticity was defined as the average ($\epsilon = 0.26$) with a position angle consistent with 0° . Afterward, thermodynamics quantities were extracted with XSPEC and fitted with `apex` and `phabs` models. The spectra were then deprojected with the tool `DSDEPROJ` (Sanders & Fabian 2007), which deprojects the spectra onto 3D ellipsoidal shells.¹⁰ Note that we varied the number of counts in each region between 3000 and 8000 and

¹⁰ Details of the code can be found at <https://www.xray.ast.cam.ac.uk/papers/dsdeproj/>.

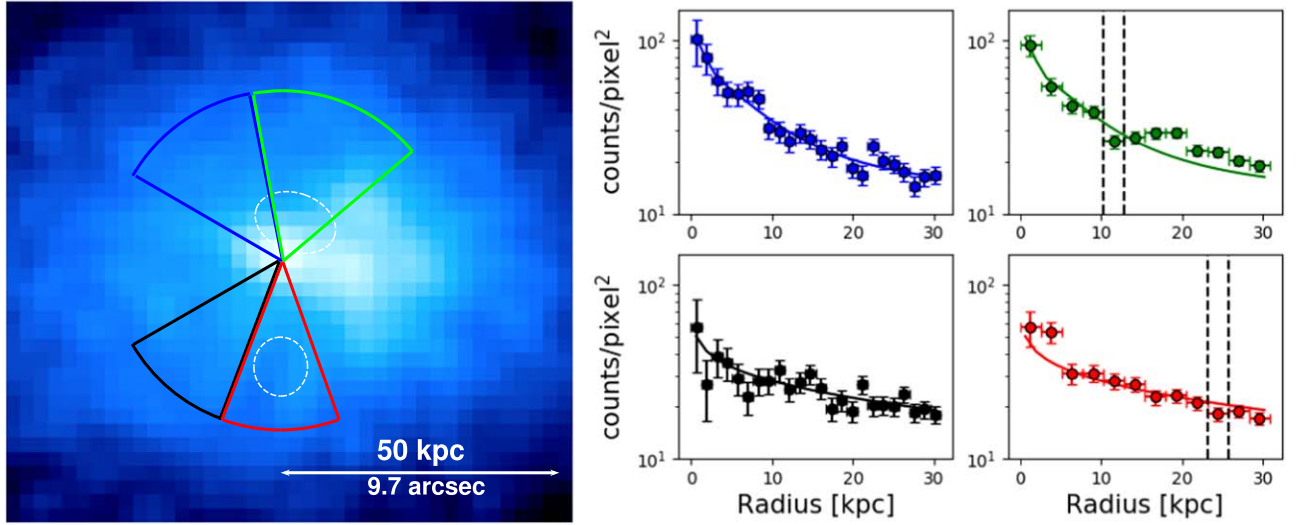


Figure 6. Left: 0.5–7 keV Chandra image of MACS J1447.4+0827 with four sectors overplotted. The white dashed ellipses denote the approximate location of the X-ray cavities. Right: double- β fitted surface brightness profile along each sector. The dashed lines denote the approximate position of the cavities.

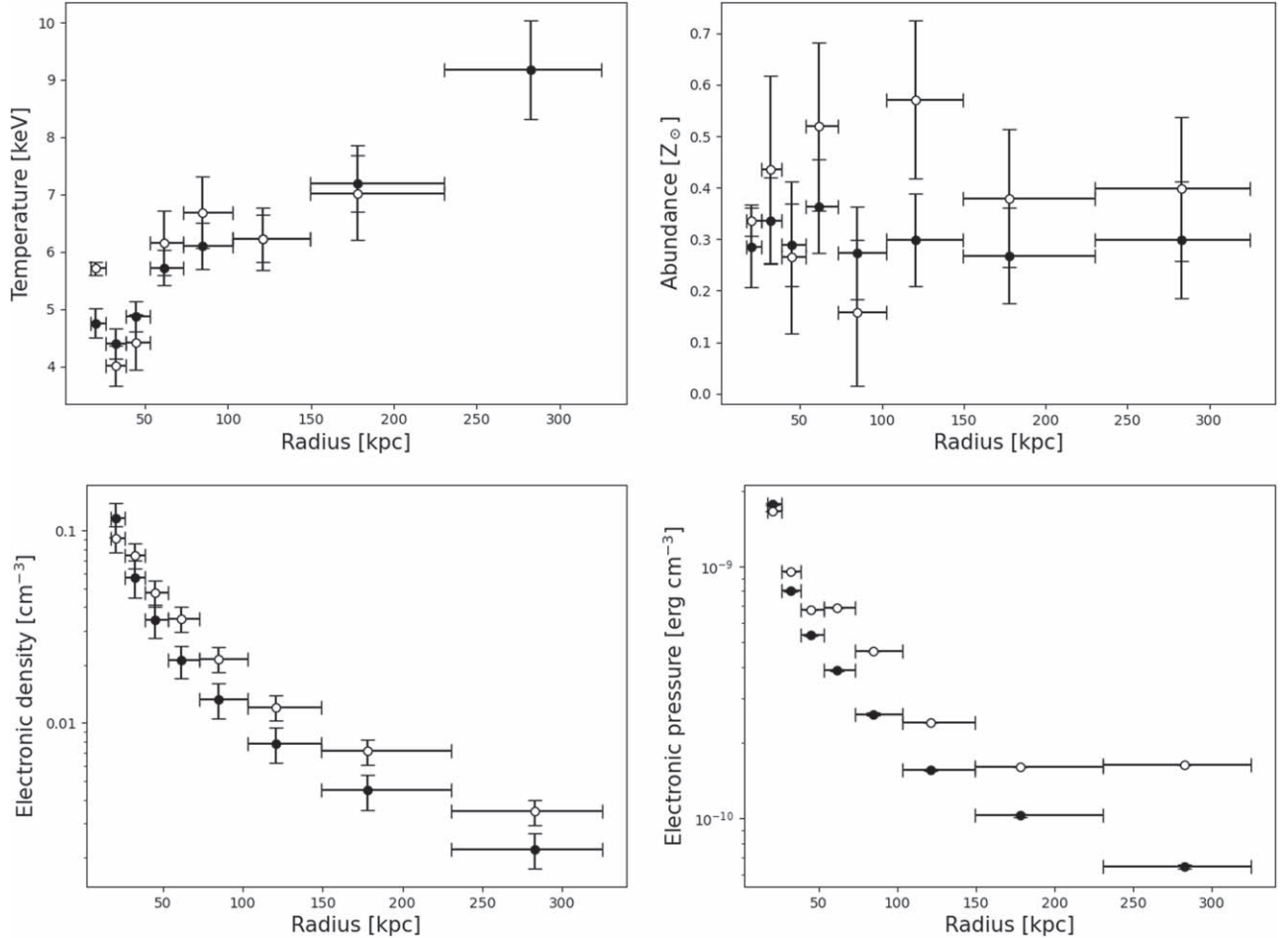


Figure 7. Projected (filled symbols) and deprojected (open symbols) temperature (top left), abundance (top right), electron density (bottom left), and electron pressure (bottom right) profiles using the method described in Section 4.1. Horizontal error bars indicate the radial extent of the bins used for fitting. Since we have a elliptical geometry, the radius is equal to the semimajor axis.

(The data used to create this figure are available.)

obtained similar fits. The projected and deprojected temperature, electron density, electron pressure, and abundance profiles are presented in Figure 7. We note that the temperature

is higher near the center, which is in agreement with the presence of an AGN. The sudden temperature increase at ~ 50 and ~ 300 kpc can be explained by cold fronts.

Table 3
X-Ray Properties of MACS J1447.4+0827

	Values
$L_{X\text{-ray}} (0.01\text{--}50 \text{ keV})$	$(5.31 \pm 0.02) \times 10^{45} \text{ erg s}^{-1}$
$L_{X\text{-ray}} (0.1\text{--}2.4 \text{ keV})$	$(1.24 \pm 0.01) \times 10^{45} \text{ erg s}^{-1}$
R_{cool}	$\sim 133 \text{ kpc}$
L_{cool}	$(1.71 \pm 0.01) \times 10^{45} \text{ erg s}^{-1}$
\dot{M}_{cool}	$< 96 M_{\odot} \text{ yr}^{-1}$

Using the deprojected temperature and density profiles, we calculated the core entropy, K_0 , based on the following equation:

$$K = kT n_e^{-2/3}. \quad (2)$$

Here kT is the gas temperature and n_e is the electron density. To calculate K_0 , we used the deprojected central density of Figure 7. The temperature is, however, strongly influenced by the AGN, so we extrapolated it using the relation $T \propto r^b$, where r is the radius and $b \sim 0.3$ (Voigt & Fabian 2004). We obtained a core entropy of $K_0 = (12 \pm 2) \text{ keV cm}^2$. According to Cavagnolo et al. (2008), this result is another confirmation that MACS J1447.4+0827 is a very strong cool core cluster, with K_0 well under 30 keV cm^2 , the threshold for cool core clusters.

Similar to the steps described in this section, we extracted the X-ray luminosity of the nine regions using XSPEC in order to compute the cooling time profile. The model `clumin`, which calculates X-ray luminosity between 0.01 and 50 keV, was used, and the data were deprojected using `projct`. The luminosity between 0.1 and 2.4 keV was also calculated (see Table 3 for the values). The cooling time arises from the following equation:

$$t_{\text{cool}} = \frac{5}{2} \frac{1.9 n_e kT V}{L_X}, \quad (3)$$

where n_e is the electronic density, kT is the gas temperature, V is the gas volume contained within an annulus, and L_X is the gas X-ray luminosity. We define the cooling radius (R_{cool}) as the radius for which the cooling time is equal to the $z = 1$ look-back time ($t_{\text{cool}} = 7.7 \text{ Gyr}$; represented by a dashed horizontal line in Figure 8), same as Rafferty et al. (2006). We define the cooling luminosity (L_{cool}) as the X-ray luminosity contained within R_{cool} between 0.1 and 2.4 keV. We extracted the X-ray luminosity within an ellipsoid with a semimajor axis of $a = R_{\text{cool}}$ and an ellipticity of $\epsilon = 0.26$. This gives us $R_{\text{cool}} \approx 133 \text{ kpc}$ and $L_{\text{cool}} = (1.71 \pm 0.01) \times 10^{45} \text{ erg s}^{-1}$ (see Table 3). We further analyze the implications of those results in Section 7.2.

In Figure 8, we present the cooling time profiles of 91 cool core clusters from the ACCEPT sample and the Phoenix cluster (McDonald et al. 2019), in which we overplotted MACS J1447.4+0827 and the average t_{cool} profile for the South Pole Telescope (SPT) clusters (Sanders et al. 2018). Note that we kept the ACCEPT t_{cool} results, although they might not be accurate (e.g., Panagoulia et al. 2014), since they are frequently used in the literature and are here used as background only. We come to the conclusion that MACS J1447.4+0827 is one of the strongest cool core clusters known. The central point is influenced by the central AGN.

Furthermore, we added the model `mkcflow` based on Mushotzky & Szymkowiak (1988) to calculate the mass deposition rate (\dot{M}_{cool}) within the cooling radius R_{cool} . We set the minimal temperature to 0.1 keV and the maximal temperature and abundance to the `apec` parameters. We obtained a 3σ upper limit (see Table 3).

4.2. Thermodynamic Maps

In order to investigate the temperature and metal abundance distribution across the cluster, we generated thermodynamic maps using a technique mimicking that of Kirkpatrick & McNamara (2015). We first used a weighted Voronoi tessellation (WVT) algorithm (Cappellari & Copin 2003; Diehl & Statler 2006) to bin the 0.5–7 keV background-subtracted merged X-ray image. The WVT algorithm bins the image into similar signal-to-noise regions by first applying a bin accretion algorithm to the pixels in the image. The bin accretion map is then used as an initial guess for the true WVT algorithm, which minimizes a predetermined scale length in order to more accurately group the pixels. The final result is a geometrically unbiased image of binned structures meeting a minimal signal-to-noise requirement. This technique has been implemented by us in `python v3.6` and can be found at <https://github.com/crhea93/AstronomyTools> under the WVT repository.

With our pixel-binning scheme determined by the WVT algorithm, we must, for each individual observation, extract a spectrum corresponding to each bin. Once extracted for each bin, we simultaneously fit the three observations using XSPEC v12.10.1, Sherpa v1, and `python v3.5`. Python provided the main wrapping language, Sherpa enabled the use of well-developed fitting algorithms, and XSPEC supplied the requisite astrophysical models: `phabs` and `apec`. Constraining the redshift and column density, n_H , to the previously mentioned values in Section 2, we allow the temperature, metal abundance, and normalization to be free. We employ the `c-statistic` determined by Sherpa in addition to the Nelder–Mead optimization algorithm. The entire temperature and abundance fitting algorithm can be found in its generalized form at <https://github.com/crhea93/AstronomyTools> under the Temperature Map Pipeline repository.

The large-scale (signal-to-noise ratio of 50, $\sim 2500 \text{ counts bin}^{-1}$) and small-scale (signal-to-noise ratio of 40, $\sim 1600 \text{ counts bin}^{-1}$) temperature and abundance maps are presented in Figure 9. We note that the temperature drops abruptly at the center by a factor of ~ 3 , which is consistent with a cool core. Those maps are also coherent with the thermodynamic profiles presented in Figure 7; we observe the same drop in temperature at the center and a similar abundance distribution.

4.3. Characterization of the Plumelike Structure

As shown in the middle panel of Figure 2, the soft X-ray image reveals an extension of soft X-ray emission offset from the central AGN. It consists of a $2''.8 \times 3''.1$ plumelike structure centered at R.A. = $14^{\text{h}}47^{\text{m}}25^{\text{s}}.825$ and decl. = $+8^{\circ}28'24''.46$ that encompasses some of the optical filaments of the HST image. We extracted the abundance and temperature of the plume using `phabs` and `apec`. We obtained $T_{\text{plume}} = (4.8 \pm 0.2) \text{ keV}$ and $Z_{\text{plume}} = (0.33 \pm 0.06) Z_{\odot}$. We also extracted a region surrounding the plume and obtained $T_{\text{env}} = (5.8 \pm 0.2) \text{ keV}$ and $Z_{\text{env}} = (0.30 \pm 0.04) Z_{\odot}$. We note that the plume is statistically

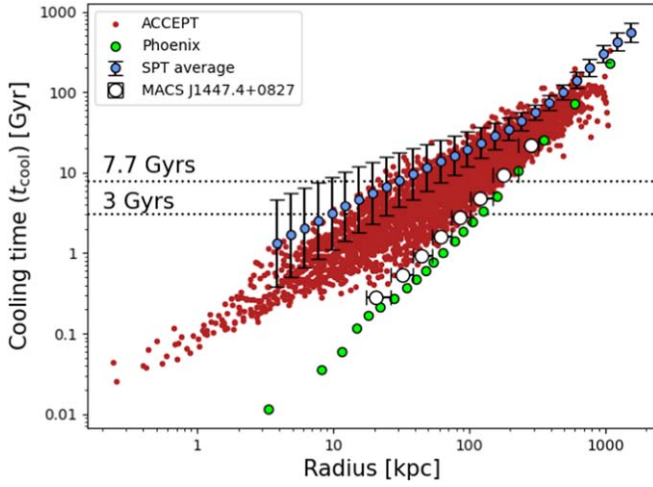


Figure 8. Average cooling time profiles for the SPT clusters (Sanders et al. 2018; blue circles), 91 cool core clusters from the ACCEPT sample (red circles), and the Phoenix cluster (green circles; McDonald et al. 2019), in which we overplotted the cooling time profile of MACS J1447.4+0827 (white circles; vertical error bars are too small to be visible), extracted from the Chandra deprojected thermodynamics quantities (for 6000 count regions). Horizontal error bars indicate the radial extent of the bins used for fitting. We added dashed horizontal lines at $t_{\text{cool}} = 3$ and 7.7 Gyr for reference. Here the cooling radius is defined as the radius where $t_{\text{cool}} = 7.7$ Gyr, which equals ~ 133 kpc.

(The data used to create this figure are available.)

colder than the surrounding medium. The colder region of the temperature map in Figure 9 also corresponds with the plumelike structure.

A more detailed description of the plumelike structure and its implications will be discussed in Section 7.3.

5. Radio Analysis of the Cluster

In Figure 3, the JVLA A-configuration observations (left panel) reveal jetted outflows oriented south–north, where each lobe extends to ~ 32 kpc in length, while the B- and C-configuration observations (middle and right panels) reveal a diffuse radio structure extending to ~ 160 kpc in size. In the following sections, we analyze these structures.

5.1. Characterization of the Relativistic Jetted Outflows

We extracted the flux of the central radio AGN and its jetted outflows using the $4\sigma_{\text{rms}}$ contours of the A-configuration observations and CASA. We extracted the flux using the tool *imstat* and estimated the error following Cassano et al. (2013),

$$\sigma_S = \sqrt{(\sigma_{\text{cal}} S)^2 + (\text{rms} \sqrt{N_{\text{beam}}})^2 + \sigma_{\text{sub}}^2}, \quad (4)$$

where S is the flux, σ_{cal} is the percentage of the flux outside of the extraction region, rms is the image noise, N_{beam} is the number of beams in the region, and σ_{sub} is the flux of point sources in the region. Here we used $\sigma_{\text{cal}} \sim 0\%$ (all of the flux is contained in the extracted region), $\text{rms} = 0.011$ mJy beam $^{-1}$, and $\sigma_{\text{sub}} = 0$ (there are no point sources).

The radio power can be calculated using the following equation:

$$P = 4\pi S D_L^2 (1+z)^{-(\alpha+1)}, \quad (5)$$

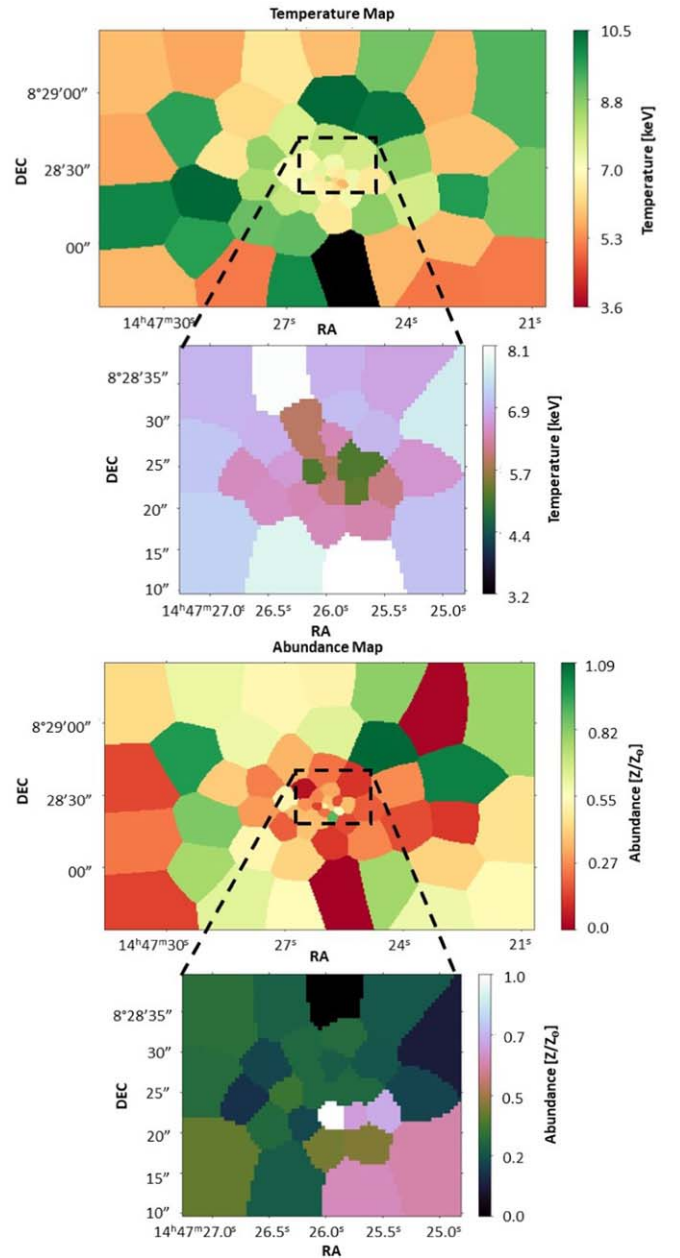


Figure 9. Large-scale temperature and abundance maps with a signal-to-noise ratio of 50 (~ 2500 counts bin $^{-1}$). The insets are small-scale maps centered on the central regions with a signal-to-noise ratio of 40 (~ 1600 counts bin $^{-1}$). The black regions signify a bin in which the fit failed to converge. Mean errors are 0.1 keV for the temperature and 0.05 Z_{\odot} for the abundance.

where D_L is the luminosity distance and α is the spectral index that characterizes the dependence of the spectra energy density S_{ν} in such a way that $S_{\nu} \propto \nu^{\alpha}$. Assuming $\alpha = -1$ for jets, we obtained $P_{\text{AGN+jets}} = (20.4 \pm 0.1) \times 10^{24}$ W Hz $^{-1}$. We compare this result with the X-ray results in Section 7.2.

5.2. Characterization of the Minihalo

A radio minihalo is a faint radio emission that has a characteristic size of 50–300 kpc found at the center of cool core clusters. Richard-Laferrière et al. (2020) already presented an initial analysis of the radio minihalo of MACS J1447.4+0827, but here we focus on characterizing its radio properties compared to the X-ray properties of the cluster.

Table 4
Radio Properties in the *L* Band (1.4 GHz)

	Values
R_{jets}	~ 32 kpc
R_{MH}	~ 160 kpc
$S_{\text{AGN+jets}}$	(39.4 ± 0.2) mJy
S_{MH}	(5.7 ± 0.5) mJy
α_{MH}	~ -1.2
$P_{\text{AGN+jets}}$	$(19.1 \pm 0.1) \times 10^{24}$ W Hz $^{-1}$
P_{MH}	$(3.0 \pm 0.3) \times 10^{24}$ W Hz $^{-1}$

The size and flux of the minihalo were calculated using the $4\sigma_{\text{rms}}$ contours of the C-configuration observations, since they contain 99% of the minihalo’s flux. The size can be found in Table 4. The tool *imstat* in *CASA* was used to extract the flux, and we used $\sigma_{\text{cal}} \sim 1\%$ (since 99% of the minihalo’s flux is inside of the extraction region), $\text{rms} = 0.015$ mJy beam $^{-1}$, and $\sigma_{\text{sub}} = 0$ (there are no point sources) to estimate the error on the flux. However, the C configuration contains the minihalo’s flux but also the AGN’s and its jets; we thus obtained the minihalo’s flux S_{MH} by subtracting the A-configuration flux ($S_{\text{AGN+jets}}$) from the C-configuration flux (S_{C} ; see Table 4 for the values).

The minihalo spectral index map of configuration C at 1.4 GHz was calculated using the tool *clean*; it uses parameters that can model the frequency dependence across the bandwidth using the first two terms of the Taylor series. The spectral map was obtained by dividing the image associated with the second term (image tt1) by the image associated with the first term (image tt0; total intensity of the 1.4 GHz image). Note that we only considered pixels detected at greater than $4\sigma_{\text{rms}}$. Taking the maximum value of a histogram of the spectral indexes of the map within a radius of $\sim R_{\text{MH}}$, we find $\alpha \sim -1.2$ for the minihalo. The power of the minihalo was calculated with Equation (5) from the previous section, and we obtained $P_{\text{MH}} = (3.0 \pm 0.3) \times 10^{24}$ W Hz $^{-1}$. We further discuss these results in Section 7.4.

Table 4 presents a summary of the radio properties of MACS J1447.4+0827.

6. The Central AGN

6.1. Radiative Properties of the Central AGN

Using the Chandra 3–8 keV image, we found evidence of a central point source whose position coincides with the brightest pixels of the HST image (R.A. = $14^{\text{h}}47^{\text{m}}26^{\text{s}}.022$, decl. = $+8^{\circ}28'25''.26$) in the BCG; this emission is characteristic of an AGN. Taking a circular region with a radius of $1''$ around the X-ray-brightest pixel in the hard 3–8 keV image, we compared the total number of counts to the 3σ upper limit of the surrounding background. We defined the surrounding background as an annular region of $3''$ of inner radius and $5''$ of outer radius. We calculated the number of counts, added 3σ , and scaled it to the number of counts expected for a small region of radius $1''$. The total number of counts of the $1''$ region is above the 3σ upper limit of the surrounding background, so the presence of an AGN is photometrically confirmed.

We furthermore calculated the hardness ratio defined as $\frac{H-S}{H+S}$, where H is the number of counts in the hard X-ray and S is the number of counts in the soft X-ray for a common region (Wang et al. 2004; Jin et al. 2006; Klesman & Sarajedini 2012). Taking the 0.5–2 and 2–8 keV images, we obtained hardness ratios of

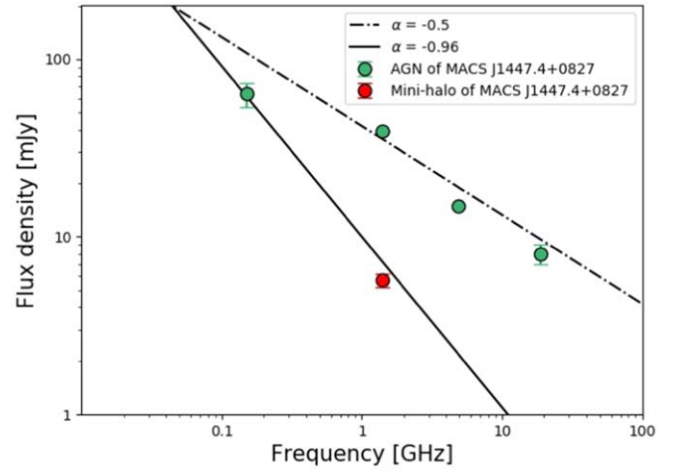


Figure 10. Radio SED of the BCG using data from TGSS, VLBA, and ATCA for frequencies different from 1.4 GHz (private communication with A. C. Edge). The flux of the minihalo (see Table 4) is also plotted. The dashed–dotted black line indicates $\alpha = -0.5$ (fitting a power law using the three green dots on the right), and the solid black line indicates $\alpha = -0.96$ (fitting a power law using the green dot on the left and the red dot).

(The data used to create this figure are available.)

-0.25 ± 0.04 for the $1''$ central region and -0.38 ± 0.01 for the $3'' \times 5''$ surrounding background. We note that the hardness ratio of the central region is 3σ above the surrounding background. We therefore confirm the presence of an X-ray-detected AGN in the BCG of MACS J1447.4+0827. We calculated the AGN’s luminosity by first fitting the spectra of an annular $3''$ – $5''$ region to *phabs*apec*. We then extrapolated the temperature to the central $1''$ region using the relation $T \propto r^b$ ($b \sim 0.3$; Voigt & Fabian 2004) and fitted a model *phabs*(powerlaw+apec)* to the region within $r = 1''$. Note that we fixed the abundance of the thermal gas and the photon index to $\Gamma = 1.9$. We obtained an unabsorbed X-ray luminosity of $L_{\text{AGN}} = 2.1 \pm 0.2 \times 10^{43}$ erg s $^{-1}$ between 2 and 10 keV. We discuss the results in Section 7.5.

6.2. Radio Spectral Energy Distribution

In Figure 10, we computed the spectral energy distribution (SED) of the cluster using the radio flux density measurements for the BCG in MACS J1447.4+0827 from our own analysis (see Section 5.1) and a private communication with Alastair C. Edge. We also plotted the minihalo’s flux (see Table 4). Hogan et al. (2015) found that the radio SED can be decomposed into two major components: an active, typically flat-spectrum component attributed to AGN activity ($\alpha > -0.5$) and a steeper component that includes all of the other emissions ($\alpha < -0.5$). We therefore plotted lines for $\alpha = -0.5$ for the three points on the right and $\alpha = -0.96$ (average steeper-spectrum emission) for the point on the left. The claimed minihalo’s flux in Table 4 is consistent with the Tata Institute of Fundamental Research (TIFR) Giant Metrewave Radio Telescope (GMRT) Sky Survey (TGSS) point. In fact, at low frequency, we see the past emission (or the jets). According to the flux equation, when the frequency decreases, the flux increases for old synchrotron emission. Consequently, the signal from the TGSS point comes from the past emission and not from the core. Also, MWA GLEAM upper limits are consistent with the $\alpha = -0.96$ line, but data from MWA or LOFAR could allow us to go deeper.

Table 5
X-Ray Cavity Properties in MACS J1447.4+0827

Cavity	R_w (kpc)	R_l (kpc)	R_{dist} (kpc)	t_{sound} (10^7 yr)	$P_{\text{cav min}}$ (10^{44} erg s $^{-1}$)	$P_{\text{cav max}}$ (10^{44} erg s $^{-1}$)	$P_{\text{cav tot}}$ (10^{44} erg s $^{-1}$)
Northern	[3.5; 4.2]	[5.0; 18.1]	9.0	0.9 ± 0.1	2.5 ± 0.4	6.3 ± 1.1	$P_{\text{cav tot}} = [2.9 \pm 0.4; 8.4 \pm 1.1]$ $P_{\text{cav tot mean}} = 5.7 \pm 0.5$
Southern	[3.2; 3.9]	[4.1; 14.7]	21.9	2.7 ± 0.2	0.40 ± 0.05	2.1 ± 0.3	

Note. The radii values indicate the minimum and maximum values from the X-ray images; same for $P_{\text{cav tot}}$.

6.3. Power of the X-Ray Cavities

Here we characterize the two X-ray cavities found in Figure 5 that coincide with the jetted outflows detected at radio wavelengths. If we assume that the cavities are in pressure equilibrium with the surrounding medium (e.g., Birzan et al. 2004), we can estimate the total energy contained in them with the following equation:

$$E_{\text{cavity}} = \frac{\gamma}{\gamma - 1} pV, \quad (6)$$

where γ is the heat capacity ratio, p is the thermal pressure, and V is the volume of the cavity. For a relativistic fluid, $\gamma = 4/3$ (Nulsen & McNamara 2013), and therefore $E_{\text{cavity}} = 4pV$.

We can approximate the volume of the cavity as $V = 4\pi R_w^2 R_l / 3$, assuming that they are ellipsoids. Here R_w and R_l are respectively defined as the projected semimajor axis perpendicular and parallel to the radio jet axis and have been measured directly based on Figure 5. Note that we assign a 20% uncertainty to R_w and R_l given the limited resolution of the X-ray data and because they are not deep enough to more clearly detect the cavities.

There are three different methods for computing the timescale associated with cavities: the buoyant rise time (Churazov et al. 2001), the refill time (McNamara et al. 2000), and the sound-crossing time, defined as

$$t_{\text{sound}} = \frac{R}{c_s}, \quad (7)$$

where c_s is the sound-crossing time of the gas ($c_s = \sqrt{\gamma kT / \mu m_H}$). It remains unclear which one is the best estimation, but since they do not vary significantly from one another, we computed the cavity powers as $4pV/t_{\text{sound}}$. Table 5 presents the results, and we further discuss the consequences in Section 7.2.

7. Discussion

7.1. The Strongest Cool Core Clusters

We have conducted an X-ray (Chandra), radio (JVLA), and optical (HST) analysis of the massive cluster MACS J1447.4+0827. It is a strong cool core and X-ray-luminous cluster. Its total mass, within a radius where the mean density is equal to 500 times the critical density at $z = 0.3755$, is estimated to be $M_{500} = (7.46_{-0.86}^{+0.80}) \times 10^{14} M_{\odot}$ (Planck Collaboration et al. 2016).

In Figure 11, we compare the 0.1–2.4 keV X-ray luminosity of MACS J1447.4+0827 to other known clusters of galaxies with similar redshifts. This plot includes clusters from MACS (Ebeling et al. 2007, 2010), the South Pole Telescope survey (Bulbul et al. 2019), and the Planck survey (Planck Collaboration et al. 2011). MACS J1447.4+0827 is one of the most X-ray-luminous clusters known in the literature.

Furthermore, in Figure 12, we compare MACS J1447.4+0827 to other strong cool core clusters. Here we plot the cooling luminosity of several known cool core clusters as a function of redshift. Most of these data were taken from Hlavacek-Larrondo et al. (2013b). While Figure 12 is not complete, we note that MACS J1447.4+0827 is one of the strongest cool core clusters around $z \approx 0.3$.

Several authors have also noted that strong cool core clusters often host a prominent abundance peak that coincides with the cool core (e.g., Ghizzardi et al. 2010; De Grandi et al. 2014). Such peaks are thought to originate from metals being created by stellar processes in the central galaxy and have even been observed in high-redshift clusters (e.g., WARPS J1415.1+3612; De Grandi et al. 2014). However, as we can see in the top right panel of Figure 7, the abundance profile of MACS J1447.4+0827 does not have a pronounced peak. The abundance profile shown in Figure 7 further shows that the metallicity varies substantially region to region. This could be explained by recent sloshing motions that disturb the metal distribution close to the BCG. In fact, when the gas sloshes back and forth in the gravitational potential, it creates temperature and abundance discontinuities (e.g., Simionescu et al. 2010). In A3526 ($z = 0.01140$), Sanders et al. (2016) showed that the sloshing motion can distort and induce asymmetries in the metal distribution across the BCG. Although MACS J1447.4+0827 has a much higher redshift than A3526, we also observed a nonuniform metal distribution in the abundance profile in Figure 7. The metal distribution may trace the history of the gas motions and provide relevant information about the sloshing mechanisms (e.g., Simionescu et al. 2010).

7.2. Relativistic Outflows and X-Ray Cavities

In Hlavacek-Larrondo et al. (2012a), the authors analyzed Chandra X-ray observations of 76 MACS clusters and found that 20 showed evidence of X-ray cavities. MACS J1447.4+0827 was found to host one potential X-ray cavity, although with the limited X-ray observations at the time (≈ 10 ks), the authors were not able to study the properties of the cavity in detail.

Here, using new deep Chandra observations, as well as new JVLA observations, we find clear evidence of two collimated jetted outflows, one of which coincides with the X-ray cavity detected by Hlavacek-Larrondo et al. (2012a). The two X-ray cavities are located symmetrically to the north and south of the central galaxy. They both have a length of ≈ 32 kpc, although they have an elliptical and not circular morphology. Interestingly, the jetted outflows are clearly detected at radio wavelengths, but they are only detected at an $\sim 2\sigma$ level compared to the surrounding X-ray background, which is not the case for other known cavities at similar redshifts.

In Kolokythas et al. (2018), the authors compared the X-ray cavity power P_{cav} to the radio power of the central AGN at

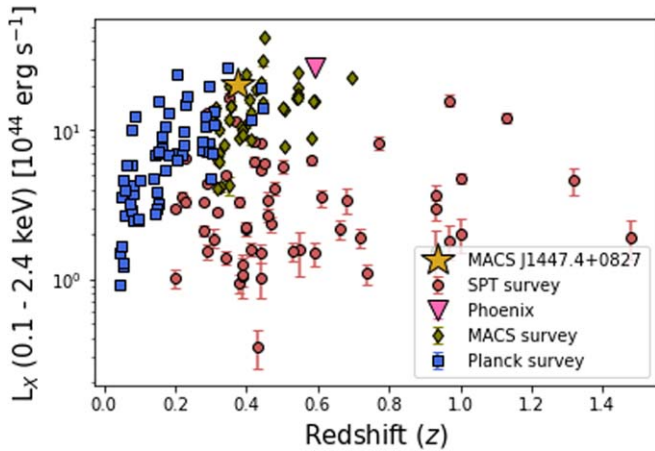


Figure 11. The X-ray luminosities in the 0.1–2.4 keV energy range for a sample of clusters from the SPT (red circles; Bulbul et al. 2019), MACS (green diamonds; Ebeling et al. 2007, 2010), and Planck (blue squares; Planck Collaboration et al. 2011) surveys. MACS J1447.4+0827 (yellow star) and Phoenix (pink triangle) are labeled. We note that MACS J1447.4+0827 is one of the X-ray brightest.

(The data used to create this figure are available.)

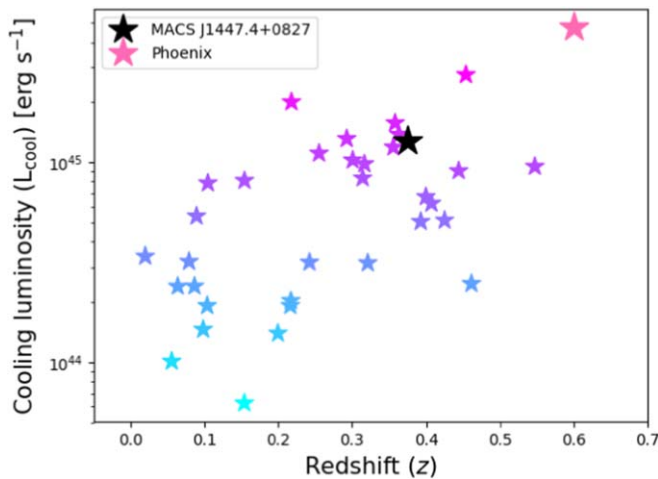


Figure 12. Cooling luminosities in the 0.1–2.4 keV energy range for a sample of strong cool core clusters from Hlavacek-Larrondo et al. (2013a). MACS J1447.4+0827 (black star) and Phoenix (pink star) are labeled.

(The data used to create this figure are available.)

235 MHz and found that the two quantities are correlated with each other. In MACS J1447.4+0827, we found that $P_{\text{cav}} \sim 6 \times 10^{44} \text{ erg s}^{-1}$ and $P_{\text{AGN+jets}} = (20.4 \pm 0.1) \times 10^{24} \text{ W Hz}^{-1}$. By converting our radio power at 1.4 GHz–235 MHz assuming $\alpha \approx -1$, we find that MACS J1447.4+0827 falls directly on the relations found by Birzan et al. (2008) and O’Sullivan et al. (2011; see Figure 7 of Kolokythas et al. 2018), implying that the radio and X-ray cavity powers in this cluster are consistent with those detected in other systems.

In Figure 13, we compare the total mechanical power of X-ray cavities to the cooling luminosity of various samples of clusters. Here the figure has been adapted from Hlavacek-Larrondo et al. (2015) and the data taken from Rafferty et al. (2006), Dunn & Fabian (2008), Nulsen et al. (2009), and Hlavacek-Larrondo et al. (2012b, 2015).

The total mechanical power of the X-ray cavities in MACS J1447.4+0827 seems to be lower than the cooling luminosity by a factor of ~ 8 . As we see in Figure 13, MACS J1447.4+0827 appears to be closer to the $E_{\text{cav}} = 16pV$ line than the $E_{\text{cav}} = 4pV$ line. This could mean that MACS J1447.4+0827 is in a phase of lower AGN power; depending on the different cycles of AGN feedback, the power of the X-ray cavities can vary, although on average, the power is sufficient to suppress cooling of the hot atmosphere. However, considering the (large) uncertainties in X-ray cavity powers, the scatter in Figure 13, and the fact that MACS J1447.4+0827 falls within this scatter, AGN feedback can easily be strong enough to offset cooling in this cluster. Therefore, AGN feedback seems to be, at the very least, present in the strongest cool core clusters at $z = 0.3$ and may still provide a viable solution to the cooling flow problem even at these redshifts.

On the right panel of Figure 5, we also note that the direction of the outflows matches the location of the northern cavity, but not exactly the southern cavity. To highlight this better, we present the combined HST F814W (red), F606W (green), and double- β -subtracted Chandra (blue) images of MACS J1447.4+0827 in Figure 14, in which we indicated the direction of the radio outflows (green arrows) and prominent optical filaments (red arrows), as well as the approximate location of the X-ray cavities (white ellipses) and ghost cavities (yellow ellipses) as seen in the unsharp-masked and double- β -subtracted Chandra images. Note that the filaments and ghost cavities are discussed in the subsequent section. The shift between the south-oriented outflow and the southern cavity is interesting and may be explained by the dynamic nature of the cluster, although deeper observations are needed to better understand this scenario.

There are a number of lines of evidence for the presence of sloshing motions in MACS J1447.4+0827. The temperature profile (Figure 7), plumelike structure (Figure 2), optical filaments (Figure 4), and prominent ellipticity of the cluster all point to a past merger event. However, as we do not detect another X-ray peak, we suspect that it was a relatively minor merger event. This merger event and the sloshing it generates could therefore induce a shift between the cool core and the BCG (Hamer et al. 2012).

7.3. Optical Filaments, Ghost Cavities, and the Plume

In Section 3, we introduced the possibility of the presence of ghost cavities, consisting of cavities that have been dragged out of the AGN’s area to larger radii. This type of cavity has been seen in other clusters at lower redshifts (e.g., A2052, Blanton et al. 2009; A2597, McNamara et al. 2001; Fornax, Su et al. 2017; A1795, Walker et al. 2014; Perseus, Hitomi Collaboration et al. 2018) but also at higher redshifts (e.g., Phoenix, McDonald et al. 2015; RX J1532.9+3021, Hlavacek-Larrondo et al. 2013a).

In Figure 14, we note that the prominent optical filaments of the cluster are oriented toward the potential ghost cavities. Optical filaments are thought to be created from thermally unstable ICM gas (e.g., McCourt et al. 2012; Sharma et al. 2012; Gaspari et al. 2013b; Li & Bryan 2014a, 2014b) that originates, in part, from the pushing-back motions created by the formation of X-ray cavities (e.g., McNamara et al. 2016; Hogan et al. 2017; Prasad et al. 2017; Voit et al. 2017; Gaspari et al. 2018). Therefore, filaments could have been created in the wake of the cavities (e.g., Hlavacek-Larrondo et al. 2013a), and thus the observed optical filaments in MACS J1447.4+0827

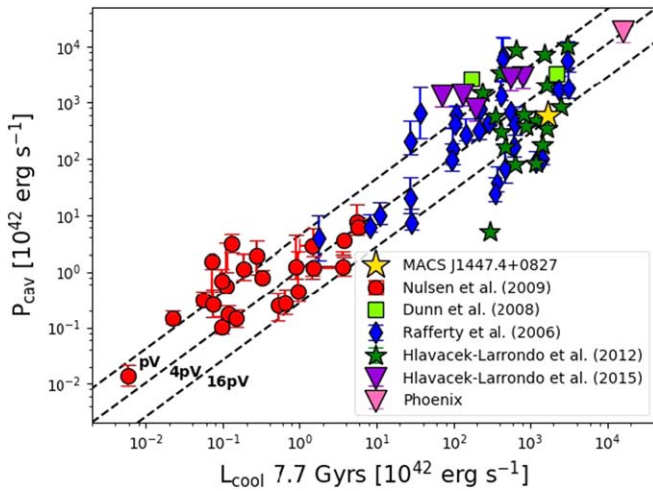


Figure 13. Total mechanical power (P_{cav}) of the X-ray cavities as a function of the cooling luminosity (L_{cool}) at 7.7 Gyr. Data from Rafferty et al. (2006) are indicated as blue diamonds, Dunn & Fabian (2008) as green squares, Nulsen et al. (2009) as red circles, Hlavacek-Larrondo et al. (2012b) as green stars, and Hlavacek-Larrondo et al. (2015) as purple triangles. MACS J1447.4+0827 (yellow star) and Phoenix (pink triangle; McDonald et al. 2019) are labeled. Dashed black lines denote $P_{\text{cav}} = L_{\text{cool}}$ for $E_{\text{cav}} = pV$, $4pV$, and $16pV$. Figure adapted from Hlavacek-Larrondo et al. (2015).

(The data used to create this figure are available.)

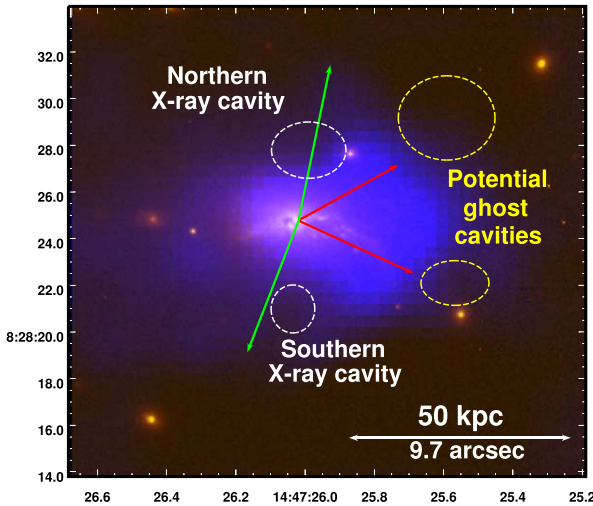


Figure 14. Combined HST F814W (red), F606W (green), and double- β -subtracted Chandra (blue) images of MACS J1447.4+0827. The green arrows show the direction of jetted outflows based on the JVLA data, and the red arrows show the prominent filaments based on the HST data. The approximate locations of the northern and southern cavities are indicated, as well as the approximate locations of the potential ghost cavities based on Figure 5.

could be created in the wake of the ghost cavities seen to the west. These X-ray cavities could have been pushed back by sloshing motions toward the western side of the cluster, implying that X-ray cavities do not just rise buoyantly but are also constantly affected by the dynamics of the X-ray gas in the cluster. Due to the evidence of sloshing motions mentioned before, the bulk of the ICM may have moved to the west, which may have caused a shift between the jets and part of the southern X-ray cavity. Such dynamic motions of the cluster

may also have shifted the position of the ghost cavities in the same direction.

In Section 4.3, we characterized the X-ray plumelike structure. We found out that the plume was colder than the environment. The origin of this type of structure is still unsure but has been observed in many clusters (e.g., A3526, Sanders & Fabian 2002; Crawford et al. 2005; Walker et al. 2015; RX J1532.9+3021, Hlavacek-Larrondo et al. 2013a; merging A2146, Russell et al. 2012). The plume would come from the gas from the regions in the BCG; the gas would have first been driven out by the cavities before falling back to the BCG (e.g., Walker et al. 2015). In their study of the optical filaments in NGC 1275, Fabian et al. (2011) proposed that the gas in the plume is excited by the ICM gas. While cooling, the hot gas from the ICM penetrates the optical cold filaments through the reconnection diffusion process, which allows the hot gas to enter the cold gas despite the magnetic field that holds the filaments. By crossing it, the gas of the ICM transfers energy to the filaments and would allow its excitation.

7.4. Radio Minihalo

There are now over 30 radio minihalos that have been discovered (see Giacintucci et al. 2019 and Richard-Laferrrière et al. 2020). The minihalo of MACS J1447.4+0827 was presented and analyzed in detail in Richard-Laferrrière et al. (2020). The minihalo’s power was plotted as a function of the 0.01–50 keV X-ray luminosity and compared to other minihalos in cool core clusters. It was found that the minihalo in MACS J1447.4+0827 follows this correlation but is one of the most radio-powerful known to date.

The exact origin of minihalos is still unknown. Like jetted outflows, their radiation is due to synchrotron emission by relativistic particles in the cluster’s magnetic field. However, the radiative lifetime of the particles is too short to spread over the observed minihalo’s radius. This implies that the particles of minihalos come from the reacceleration of relativistic particles or are produced in situ (van Weeren et al. 2019). For the latter, minihalos could come from the proton–proton interaction between the cosmic rays and the ICM (Pfrommer & Enßlin 2004; Fujita et al. 2007; Zandanel et al. 2014). For the former, it has been proposed that turbulence in the ICM could be the source of reacceleration. It was suggested that this turbulence could be caused by either the dynamics of the jets (e.g., Bravi et al. 2016; Richard-Laferrrière et al. 2020) or sloshing motions of the ICM via minor mergers (Mazzotta & Giacintucci 2008; ZuHone et al. 2013; Giacintucci et al. 2014). This kind of motion leaves traces: cold fronts, which are discontinuities of temperature and density that appear to bound the minihalos (e.g., Markevitch et al. 2001; Mazzotta et al. 2003; Markevitch & Vikhlinin 2007; Owers et al. 2009; Ghizzardi et al. 2010).

In MACS J1447.4+0827, we find evidence of two cold fronts (see top left panel of Figure 7) located at radii of ~ 50 and ~ 300 kpc. The minihalo in MACS J1447.4+0827 therefore appears to be bounded by the cold fronts, since $R_{\text{MH}} \sim 160$ kpc. However, Richard-Laferrrière et al. (2020) recently found evidence that minihalos are directly connected to the AGN feedback processes of the BCG. In this work, the power of the minihalo was plotted as a function of the BCG steep radio power at 1 GHz, the BCG core radio power at 10 GHz, and the total power of the X-ray cavities. In all cases, the minihalo of MACS J1447.4+0827 agrees with the

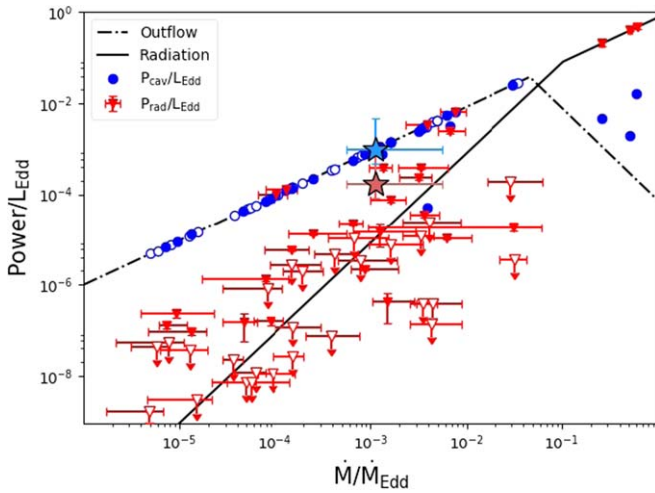


Figure 15. Cavity power (blue circles) and radiative power (red triangles) scaled by the Eddington luminosity as a function of the required mean accretion rate scaled by the Eddington rate ($\dot{M}/\dot{M}_{\text{Edd}}$). The open symbols indicate the upper limits, which are on the X-ray luminosity. Figure adapted from Russell et al. (2013). There are two points for each source. MACS J1447.4+0827 is shown by stars.

(The data used to create this figure are available.)

correlations, indicating that the minihalo in this cluster could also be connected at a fundamental level with its feedback processes.

7.5. Power Mechanisms in the Central AGN

In order to further understand the feedback mechanisms occurring in the central AGN of MACS J1447.4+0827, we computed its Eddington luminosity, the black hole’s mean accretion rate, and the Eddington rate.

The Eddington luminosity is defined as the limiting luminosity where the radiation pressure is in equilibrium with the local gravity of the accreting material. For a fully ionized plasma, the Eddington luminosity is given by the following equation:

$$\frac{L_{\text{Edd}}}{\text{erg s}^{-1}} = 1.26 \times 10^{47} \left(\frac{M_{\text{BH}}}{10^9 M_{\odot}} \right), \quad (8)$$

where M_{BH} is the SMBH mass. Since there are no mass estimates of the black hole available in the literature, we assumed a mass of between 9 and $10 \times 10^9 M_{\odot}$ for MACS J1447.4+0827, which is the typical mass expected for such a massive cluster and central galaxy.

The mean accretion rate scaled by the Eddington rate can be expressed as

$$\frac{\dot{M}}{\dot{M}_{\text{Edd}}} = \frac{(P_{\text{cav}} + L_{\text{bol}})}{L_{\text{Edd}}}, \quad (9)$$

where L_{bol} is the bolometric luminosity. Here we used a typical bolometric correction of 5 for low-luminosity sources on the 2–10 keV X-ray luminosity of the central AGN (see Section 6.1 for the value), following Russell et al. (2013).

Figure 15 presents the cavity power (blue circles) and radiative power (red triangles) scaled by the Eddington luminosity as a function of the required mean accretion rate scaled by the Eddington rate ($\dot{M}/\dot{M}_{\text{Edd}}$). The open symbols

indicate the upper limits. The figure was adapted from Russell et al. (2013; their Figure 12) and Churazov et al. (2005; their Figure 1). We plotted the location of MACS J1447.4+0827 (stars), similar to the cavity power in blue and radiative power in red.

At low accretion rates, it is the jetted outflow mode that is dominant rather than the radiative (e.g., Churazov et al. 2005; Russell et al. 2013). Indeed, Figure 15 shows that for $\dot{M}/\dot{M}_{\text{Edd}} \lesssim 3 \times 10^{-2}$, the outflow mode dominates over the radiative mode. Since MACS J1447.4+0827 is not in the quasar phase, the outflow mode dominates over the radiative mode by a factor of ~ 10 .

The radiative mode would act mainly in the young AGNs ($z \gtrsim 1$) when they are in the quasar stage and the accretion rate of the black hole is high (e.g., Churazov et al. 2005; Hopkins et al. 2006). We find that our object is perfectly consistent with the low-accretion mode, even though it is located at $z > 0.3$. We can therefore affirm that this feedback mode was in place several Gyr ago in MACS J1447.4+0827. It is also happening in many other clusters (e.g., Hlavacek-Larrondo et al. 2012b, 2015).

8. Summary and Conclusions

In this work, we have presented the first detailed and multiwavelength analysis of one of the strongest cool core clusters known, MACS J1447.4+0827 ($z = 0.3755$), using data from the HST and new data from the Chandra X-ray Observatory and the JVLA. Our relevant findings are summarized as follows.

1. MACS J1447.4+0827, with its 0.01–50 keV X-ray luminosity of $L_{\text{X}} = (5.31 \pm 0.02) \times 10^{45} \text{ erg s}^{-1}$, is one of the most luminous clusters at $z < 0.7$.
2. We detected a northern and a southern X-ray cavity, as well as two potential ghost cavities. The A-configuration JVLA observations reveal jetted outflows oriented south–north extending to ~ 32 kpc in length and coincident with the X-ray cavities. Their total mechanical power is $P_{\text{cav}} \approx 6 \times 10^{44} \text{ erg s}^{-1}$.
3. We calculated the cooling luminosity of $L_{\text{cool}} = (1.71 \pm 0.01) \times 10^{45} \text{ erg s}^{-1}$. This cooling luminosity indicates that MACS J1447.4+0827 is one of the strongest cool core clusters around $z < 0.7$. We found that the total mechanical power of the X-ray cavities was generally consistent with the power required to offset the cooling of the ICM. MACS J1447.4+0827 might currently be going through a phase of lower activity, but not to the point of leading to a catastrophic cooling of the core.
4. The HST images reveal an elliptic BCG in the center of MACS J1447.4+0827, as well as large $\text{H}\alpha$ filaments whose directions match the location of the potential ghost cavities. Part of these filaments also matches the position of a cool X-ray plume.
5. The B- and C-configuration JVLA observations reveal a diffuse radio structure extending to ~ 160 kpc in size interpreted as a minihalo. The total radio power is $P_{1.4\text{GHz}} = (3.0 \pm 0.3) \times 10^{24} \text{ W Hz}^{-1}$. It is one of the most powerful minihalos found.

While this study clearly shows that powerful mechanical feedback is occurring in the strongest cool core clusters, new and/or deeper observations in other wavelengths, such as

submillimeter, infrared, optical, and ultraviolet—with the Multi Unit Spectroscopic Explorer—could provide more information concerning the star formation rate and the quantity and location of molecular gas in the BCG and would allow a better understanding of the multiphase gas in extreme cool core clusters.

We wish to thank M. McDonald for sharing his data and for his help.

M.P.E. is supported by the Natural Sciences and Engineering Research Council of Canada (NRSEC) and Fonds de recherche du Québec—Nature et technologies (FRQNT) through the Undergraduate Student Research Awards and by the Institute for Data Valorization (IVADO) through the Summer Internship and Undergraduate Research Fellowships. J.H.L. is supported by NSERC through the Canada Research Chair programs and wishes to acknowledge the support of an NSERC Discovery Grant and the FRQNT. A.R.L. is supported by NSERC through the NSERC Alexander-Graham-Bell Canada Graduate Scholarships-Master’s Program (CGS M) and FRQNT through the FRQNT Graduate Studies Research Scholarship—M. Sc. level under grant No. 209839.

ORCID iDs

M. Prasow-Émond  <https://orcid.org/0000-0002-2457-3431>

J. Hlavacek-Larrondo  <https://orcid.org/0000-0001-7271-7340>


C. L. Rhea  <https://orcid.org/0000-0003-2001-1076>

M.-L. Gendron-Marsolais  <https://orcid.org/0000-0002-7326-5793>

A. Richard-Laferrrière  <https://orcid.org/0000-0001-7597-270X>

J. S. Sanders  <https://orcid.org/0000-0003-2189-4501>

A. C. Edge  <https://orcid.org/0000-0002-3398-6916>

A. von der Linden  <https://orcid.org/0000-0002-3881-7724>

References

- Anders, E., & Grevesse, N. 1989, *GeCoA*, **53**, 197
- Applegate, D. E., Mantz, A., Allen, S. W., et al. 2016, *MNRAS*, **457**, 1522
- Applegate, D. E., von der Linden, A., Kelly, P. L., et al. 2014, *MNRAS*, **439**, 48
- Birzan, L., McNamara, B. R., Nulsen, P. E. J., Carilli, C. L., & Wise, M. W. 2008, *ApJ*, **709**, 546
- Birzan, L., Rafferty, D. A., McNamara, B. R., Wise, M. W., & Nulsen, P. E. J. 2004, *ApJ*, **607**, 800
- Blanton, E. L., Randall, S. W., Douglass, E. M., et al. 2009, *ApJL*, **697**, L95
- Bravi, L., Gitti, M., & Brunetti, G. 2016, *MNRAS*, **455**, L41
- Bulbul, E., Chiu, I.-N., Mohr, J. J., et al. 2019, *ApJ*, **871**, 50
- Cappellari, M., & Copin, Y. 2003, *MNRAS*, **342**, 345
- Cassano, R., Ettori, S., Brunetti, G., et al. 2013, *ApJ*, **777**, 141
- Castillo-Morales, A., & Schindler, S. 2003, *A&A*, **403**, 433
- Cavagnolo, K. W., Donahue, M., Voit, G. M., & Sun, M. 2008, *ApJL*, **683**, L107
- Cavagnolo, K. W., McNamara, B. R., Nulsen, P. E. J., et al. 2010, *ApJ*, **720**, 1066
- Cavaliere, A., & Fusco-Femiano, R. 1976, *A&A*, **500**, 95
- Chirivì, G., Suyu, S. H., Grillo, C., et al. 2018, *A&A*, **614**, A8
- Churazov, E., Brüggemann, M., Kaiser, C. R., Böhringer, H., & Forman, W. 2001, *ApJ*, **554**, 261
- Churazov, E., Sazonov, S., Sunyaev, R., et al. 2005, *MNRAS*, **363**, L91
- Crawford, C. S., Hatch, N. A., Fabian, A. C., & Sanders, J. S. 2005, *MNRAS*, **363**, 216
- De Grandi, S., Santos, J. S., Nonino, M., et al. 2014, *A&A*, **567**, A102
- Diehl, S., & Statler, T. S. 2006, *MNRAS*, **368**, 497
- Dong, X.-B., Ho, L. C., Wang, J.-G., et al. 2010, *ApJL*, **721**, L143
- Dunn, R. J. H., & Fabian, A. C. 2006, *MNRAS*, **373**, 959
- Dunn, R. J. H., & Fabian, A. C. 2008, *MNRAS*, **385**, 757
- Ebeling, H., Barrett, E., Donovan, D., et al. 2007, *ApJL*, **661**, L33
- Ebeling, H., Edge, A. C., & Henry, J. P. 2001, *ApJ*, **553**, 668
- Ebeling, H., Edge, A. C., Mantz, A., et al. 2010, *MNRAS*, **407**, 83
- Ehlert, S., Allen, S., von der Linden, A., et al. 2011, *MNRAS*, **411**, 1641
- Fabian, A. C. 1994, *ARA&A*, **32**, 277
- Fabian, A. C., Sanders, J. S., Williams, R. J. R., et al. 2011, *MNRAS*, **417**, 172
- Farrah, D., Baloković, M., Stern, D., et al. 2016, *ApJ*, **831**, 76
- Franceschini, A., Bassani, L., Cappi, M., et al. 2000, *A&A*, **353**, 910
- Fujita, Y., Kohri, K., Yamazaki, R., & Kino, M. 2007, *ApJL*, **663**, L61
- Gaspari, M., Brighenti, F., & Ruszkowski, M. 2013a, *AN*, **334**, 394
- Gaspari, M., McDonald, M., Hamer, S. L., et al. 2018, *ApJ*, **854**, 167
- Gaspari, M., Ruszkowski, M., & Oh, S. P. 2013b, *MNRAS*, **432**, 3401
- Ghizzardi, S., Rossetti, M., & Molendi, S. 2010, *A&A*, **516**, A32
- Giacintucci, S., Markevitch, M., Brunetti, G., et al. 2014, *ApJ*, **795**, 73
- Giacintucci, S., Markevitch, M., Cassano, R., et al. 2019, *ApJ*, **880**, 70
- Gitti, M., Feretti, L., & Schindler, S. 2006, *A&A*, **448**, 853
- Gupta, A., Yuan, T., Tran, K.-V. H., et al. 2016, *ApJ*, **831**, 104
- Hamer, S. L., Edge, A. C., Swinbank, A. M., et al. 2012, *MNRAS*, **421**, 3409
- Hines, D. C., & Wills, B. J. 1993, *ApJ*, **415**, 82
- Hitomi Collaboration, Aharonian, F., Akamatsu, H., et al. 2018, *PASJ*, **70**, 9
- Hlavacek-Larrondo, J., Allen, S. W., Taylor, G. B., et al. 2013a, *ApJ*, **777**, 163
- Hlavacek-Larrondo, J., Fabian, A. C., Edge, A. C., et al. 2012a, *MNRAS*, **421**, 1360
- Hlavacek-Larrondo, J., Fabian, A. C., Edge, A. C., et al. 2013b, *MNRAS*, **431**, 1638
- Hlavacek-Larrondo, J., Fabian, A. C., Edge, A. C., & Hogan, M. T. 2012b, *MNRAS*, **424**, 224
- Hlavacek-Larrondo, J., McDonald, M., Benson, B. A., et al. 2015, *ApJ*, **805**, 35
- Hogan, M. T., Edge, A. C., Hlavacek-Larrondo, J., et al. 2015, *MNRAS*, **453**, 1201
- Hogan, M. T., McNamara, B. R., Pulido, F. A., et al. 2017, *ApJ*, **851**, 66
- Hopkins, P. F., Hernquist, L., Cox, T. J., et al. 2006, *ApJS*, **163**, 1
- Iwasawa, K., Fabian, A. C., & Ettori, S. 2001, *MNRAS*, **321**, L15
- Jauzac, M., Jullo, E., Kneib, J.-P., et al. 2012, *MNRAS*, **426**, 3369
- Jetzer, P., Koch, P., Piffaretti, R., Puy, D., & Schindler, S. 2002, arXiv:astro-ph/0201421
- Jin, Y. K., Zhang, S. N., & Wu, J. F. 2006, *ApJ*, **653**, 1566
- Johnstone, R. M., Fabian, A. C., & Nulsen, P. E. J. 1987, *MNRAS*, **224**, 75
- Jones, C., & Forman, W. 1984, *ApJ*, **276**, 38
- Kalberla, P. M. W., Burton, W. B., Hartmann, D., et al. 2005, *A&A*, **440**, 775
- Kaurov, A. A., Dai, L., Venumadhav, T., Miralda-Escudé, J., & Frye, B. 2019, *ApJ*, **880**, 58
- Kirkpatrick, C. C., & McNamara, B. R. 2015, *MNRAS*, **452**, 4361
- Kleinmann, S. G., Hamilton, D., Keel, W. C., et al. 1988, *ApJ*, **328**, 161
- Klesman, A. J., & Sarajedini, V. L. 2012, *MNRAS*, **425**, 1215
- Kolokythas, K., O’Sullivan, E., Raychaudhury, S., et al. 2018, *MNRAS*, **481**, 1550
- Li, Y., & Bryan, G. L. 2014a, *ApJ*, **789**, 153
- Li, Y., & Bryan, G. L. 2014b, *ApJ*, **789**, 54
- Limousin, M., Ebeling, H., Richard, J., et al. 2012, *A&A*, **544**, A71
- Markevitch, M., & Vikhlinin, A. 2007, *PhR*, **443**, 1
- Markevitch, M., Vikhlinin, A., & Mazzotta, P. 2001, *ApJL*, **562**, L153
- Mazzotta, P., Edge, A., & Markevitch, M. 2003, *ApJ*, **596**, 190
- Mazzotta, P., & Giacintucci, S. 2008, *ApJL*, **675**, L9
- McConnell, N. J., Ma, C.-P., Gebhardt, K., et al. 2011, *Natur*, **480**, 215
- McCourt, M., Sharma, P., Quataert, E., & Parrish, I. J. 2012, *MNRAS*, **419**, 3319
- McDonald, M., Gaspari, M., McNamara, B. R., & Tremblay, G. R. 2018, *ApJ*, **858**, 45
- McDonald, M., McNamara, B. R., van Weeren, R. J., et al. 2015, *ApJ*, **811**, 111
- McDonald, M., McNamara, B. R., Voit, G. M., et al. 2019, *ApJ*, **885**, 63
- McNamara, B. R., Russell, H. R., Nulsen, P. E. J., et al. 2016, *ApJ*, **830**, 79
- McNamara, B. R., Wise, M., Nulsen, P. E. J., et al. 2000, *ApJL*, **534**, L135
- McNamara, B. R., Wise, M. W., Nulsen, P. E. J., et al. 2001, *ApJL*, **562**, L149
- Mushotzky, R. F., & Szymkowiak, A. E. 1988, in Proc. NATO Advanced Research Workshop: Cooling Flows in Clusters and Galaxies, ed. A. C. Fabian (Dordrecht: Kluwer), **53**
- Nulsen, P., Jones, C., Forman, W., et al. 2009, in The Monster’s Fiery Breath: Feedback in Galaxies, Groups, and Clusters, ed. S. Heinz & E. Wilcots (Melville, NY: AIP)
- Nulsen, P. E. J., Johnstone, R. M., & Fabian, A. C. 1987, *PASAu*, **7**, 132
- Nulsen, P. E. J., & McNamara, B. R. 2013, *AN*, **334**, 386
- O’Dea, C. P., Baum, S. A., Privon, G., et al. 2008, *ApJ*, **681**, 1035
- O’Sullivan, E., Giacintucci, S., David, L. P., et al. 2011, *ApJ*, **735**, 11

- Owers, M. S., Nulsen, P. E. J., Couch, W. J., & Markevitch, M. 2009, *ApJ*, **704**, 1349
- Panagoulia, E. K., Fabian, A. C., & Sanders, J. S. 2014, *MNRAS*, **438**, 2341
- Peterson, J. R., & Fabian, A. C. 2006, *PhR*, **427**, 1
- Pfrommer, C., & Enßlin, T. A. 2004, *A&A*, **413**, 17
- Piconcelli, E., Fiore, F., Nicastro, F., et al. 2007, *A&A*, **473**, 85
- Planck Collaboration, Ade, P. A. R., Aghanim, N., et al. 2016, *A&A*, **594**, A14
- Planck Collaboration C., Ade, P. a. R., Aghanim, N., et al. 2011, *A&A*, **536**, A11
- Prasad, D., Sharma, P., & Babul, A. 2017, *MNRAS*, **471**, 1531
- Rafferty, D. A., McNamara, B. R., & Nulsen, P. E. J. 2008, *ApJ*, **687**, 899
- Rafferty, D. A., McNamara, B. R., Nulsen, P. E. J., & Wise, M. W. 2006, *ApJ*, **652**, 216
- Richard-Laferrrière, A., Hlavacek-Larrondo, J., Latulippe, M., et al. 2020, *MNRAS*, submitted (arXiv:2007.01306)
- Russell, H. R., McNamara, B. R., Edge, A. C., et al. 2013, *MNRAS*, **432**, 530
- Russell, H. R., McNamara, B. R., Sanders, J. S., et al. 2012, *MNRAS*, **423**, 236
- Sanders, J. S., & Fabian, A. C. 2002, *MNRAS*, **331**, 273
- Sanders, J. S., & Fabian, A. C. 2007, *MNRAS*, **381**, 1381
- Sanders, J. S., Fabian, A. C., Russell, H. R., & Walker, S. A. 2018, *MNRAS*, **474**, 1065
- Sanders, J. S., Fabian, A. C., Taylor, G. B., et al. 2016, *MNRAS*, **457**, 82
- Santos, J. S., Balestra, I., Tozzi, P., et al. 2016, *MNRAS*, **456**, L99
- Schindler, S., Castillo-Morales, A., De Filippis, E., Schwobe, A., & Wambsganss, J. 2001, *A&A*, **376**, L27
- Sharma, P., McCourt, M., Quataert, E., & Parrish, I. J. 2012, *MNRAS*, **420**, 3174
- Simionescu, A., Werner, N., Forman, W. R., et al. 2010, *MNRAS*, **405**, 91
- Smith, G. P., Ebeling, H., Limousin, M., et al. 2009, *ApJL*, **707**, L163
- Su, Y., Nulsen, P. E. J., Kraft, R. P., et al. 2017, *ApJ*, **847**, 94
- van Weeren, R. J., de Gasperin, F., Akamatsu, H., et al. 2019, *SSRv*, **215**, 16
- Vignali, C., Piconcelli, E., Lanzuisi, G., et al. 2011, *MNRAS*, **416**, 2068
- Vikhlinin, A., Markevitch, M., Murray, S. S., et al. 2005, *ApJ*, **628**, 655
- Voigt, L. M., & Fabian, A. C. 2004, *MNRAS*, **347**, 1130
- Voit, G. M., Meece, G., Li, Y., et al. 2017, *ApJ*, **845**, 80
- von der Linden, A., Mantz, A., Allen, S. W., et al. 2014, *MNRAS*, **443**, 1973
- Walker, S. A., Fabian, A. C., & Kosec, P. 2014, *MNRAS*, **445**, 3444
- Walker, S. A., Kosec, P., Fabian, A. C., & Sanders, J. S. 2015, *MNRAS*, **453**, 2481
- Wang, J. X., Malhotra, S., Rhoads, J. E., & Norman, C. A. 2004, *ApJL*, **612**, L109
- Zandanel, F., Pfrommer, C., & Prada, F. 2014, *MNRAS*, **438**, 124
- Zhuravleva, I., Allen, S. W., Mantz, A., & Werner, N. 2018, *ApJ*, **865**, 53
- Zhuravleva, I., Churazov, E., Arévalo, P., et al. 2016, *MNRAS*, **458**, 2902
- Zhuravleva, I., Churazov, E., Schekochihin, A. A., et al. 2014, *Natur*, **515**, 85
- Zitrin, A., Broadhurst, T., Rephaeli, Y., & Sadeh, S. 2009, *ApJL*, **707**, L102
- ZuHone, J. A., Markevitch, M., Brunetti, G., & Giacintucci, S. 2013, *ApJ*, **762**, 78